

# Comparison of Linear Response Theory, Projected Initial Maximum Overlap Method, and Molecular Dynamics-Based Vibronic Spectra: The Case of Methylene Blue

Ali Abou Taka, Shao-Yu Lu, Duncan Gowland, Tim J. Zuehlsdorff, Hector H. Corzo, Aurora Pribram-Jones, Liang Shi, Hrant P. Hratchian,\* and Christine M. Isborn\*



Cite This: *J. Chem. Theory Comput.* 2022, 18, 3039–3051



Read Online

ACCESS |



Metrics & More

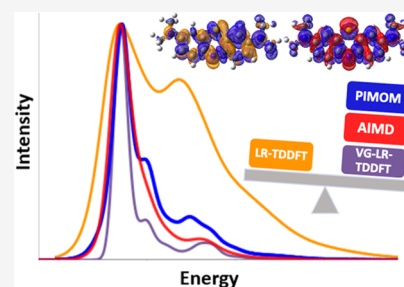


Article Recommendations



Supporting Information

**ABSTRACT:** The simulation of optical spectra is essential to molecular characterization and, in many cases, critical for interpreting experimental spectra. The most common method for simulating vibronic absorption spectra relies on the geometry optimization and computation of normal modes for ground and excited electronic states. In this report, we show that the utilization of such a procedure within an adiabatic linear response (LR) theory framework may lead to state mixings and a breakdown of the Born–Oppenheimer approximation, resulting in a poor description of absorption spectra. In contrast, computing excited states via a self-consistent field method in conjunction with a maximum overlap model produces states that are not subject to such mixings. We show that this latter method produces vibronic spectra much more aligned with vertical gradient and molecular dynamics (MD) trajectory-based approaches. For the methylene blue chromophore, we compare vibronic absorption spectra computed with the following: an adiabatic Hessian approach with LR theory-optimized structures and normal modes, a vertical gradient procedure, the Hessian and normal modes of maximum overlap method-optimized structures, and excitation energy time-correlation functions generated from an MD trajectory. Because of mixing between the bright  $S_1$  and dark  $S_2$  surfaces near the  $S_1$  minimum, computing the adiabatic Hessian with LR theory and time-dependent density functional theory with the B3LYP density functional predicts a large vibronic shoulder for the absorption spectrum that is not present for any of the other methods. Spectral densities are analyzed and we compare the behavior of the key normal mode that in LR theory strongly couples to the optical excitation while showing  $S_1/S_2$  state mixings. Overall, our study provides a note of caution in computing vibronic spectra using the excited-state adiabatic Hessian of LR theory-optimized structures and also showcases three alternatives that are less sensitive to adiabatic state mixing effects.



## 1. INTRODUCTION

The excited states of chromophores play an important role in a wide variety of applications, including solar energy capture, photocatalysis, bioluminescence/fluorescence, and electro-optic materials.<sup>1–6</sup> Predicting optical spectra and accurately characterizing excited-state potential energy surfaces (PESs) presents a challenge near regions of a conical intersection as the Born–Oppenheimer approximation becomes less valid. Adiabatic excited-state methods that allow mixing of excited states can produce PESs that strongly deviate from the harmonic curvature in the regions of state crossings. Additionally, along an adiabatic surface that might mix excited states of different character, the nature of the state may change near regions of a conical intersection. Diabatic surfaces are less well-defined, but have consistent character in the regions of surface crossings and are often useful for nonadiabatic dynamics simulations.

Because of its efficiency and relatively black box implementation, linear response (LR) theory in conjunction with time-dependent density functional theory (TDDFT) is the method of choice for most excited-state calculations, including those needed for modeling optical spectroscopy.<sup>7–9</sup> LR theory avoids

the computation of a wave function by computing excitation energies and transition densities through the LR formalism, defining all properties by the response of the energy or action functional.<sup>10</sup> Although many studies have demonstrated the ability of LR-TDDFT to accurately describe valence excited states with a single-excitation character (see ref 11 and references therein), the adiabatic excited states of a system built from solving the TDDFT matrix equations derived from first-order time-dependent perturbation theory and LR theory fail to accurately describe excited states with double-excitation character, so will inadequately describe the PES for such states.<sup>12–17</sup>

Received: November 8, 2021

Published: April 26, 2022



The  $\Delta$  self-consistent field ( $\Delta$ SCF) family of methods presents an alternative to LR methods for computing excited states.<sup>18–24,67</sup> For nonadiabatic dynamics, similar approaches based on constrained DFT have been shown to present a viable path forward for computing excited-state couplings and properties, and locating conical intersections.<sup>24–29</sup> A significant challenge of  $\Delta$ SCF is converging single-determinant representations of excited states using ground-state methods without collapsing to the ground state. In recent years, Gill and co-workers have rejuvenated work in this area using maximum overlap concepts.<sup>18,67</sup> Maximum overlap methodologies (MOMs) modify standard ground-state SCF algorithms to maximize the overlap between the occupied molecular orbitals (MOs) of a user-defined SCF target and that computed in the current SCF iteration. The projected initial maximum overlap method (PIMOM) has recently been shown to be a robust member of the family of MOM algorithms.<sup>17</sup> In this MOM variant, convergence toward an SCF solution corresponding to a user-defined electronic structure, which could represent an electronic excited state, is driven by introducing a projection operator that aims to preserve MO occupations corresponding to the target state of interest.<sup>17</sup> Importantly, MOM approaches do not introduce constraints on the SCF procedure. Rather, such schemes are meant to guide the SCF optimizer toward non-minima in the SCF space. As such, MOM-based simulations do not artificially impose symmetry or other constraints on the wave function (other than the inherent limitations of a single-determinant representation) or the geometry optimization. In recent years, MOM-based calculations have successfully been used to study valence excitation energies, excited-state geometries and vibrational frequencies, core-level excitations, and ionization energies.<sup>17,18,24,30–42,67</sup>

Vibronic spectra can be computed with a variety of methods.<sup>43–46,100</sup> Perhaps the most popular method for larger molecules is to parametrize harmonic potentials by computing the Hessian and then using the frequencies and displacements from normal modes computed at the ground- and excited-state minima, which takes the form of a generalized Brownian oscillator model (GBOM). Within this harmonic approximation to the PES, the nuclear wave functions are known, and overlaps can be calculated between ground- and excited-state wave functions to determine the intensity of vibronic transitions, yielding the exact Franck–Condon spectrum for the harmonic surfaces.<sup>47</sup> This Hessian-based approach can easily accommodate Duschinsky effects or normal mode mixing upon electronic excitation.<sup>48</sup>

The substantial computational cost associated with the excited-state Hessian calculation is avoided with the vertical gradient approach, where the excited-state nuclear derivatives are computed at the ground-state minimum and the normal modes and frequencies are assumed to be the same for the excited state as in the ground state.<sup>49,50,77</sup> By avoiding calculation of the Hessian at the excited-state minimum, the vertical gradient method is less sensitive to the presence of a conical intersection in this region.<sup>51,52</sup> In a study by Avila Ferrer and Santoro comparing vertical gradient and adiabatic Hessian approaches for the computation of vibronic spectra, the authors concluded that discrepancies in the vibronic spectra of these two methods are diagnostic of the failure of the harmonic approximation and/or a breakdown of the Born–Oppenheimer approximation due to geometry-dependent mixing of states.<sup>53</sup>

An alternative approach to the direct computation of wave function overlap as described above is the use of energy gap

time-correlation functions within a cumulant expansion of the LR function.<sup>54</sup> These energy gap time-correlation functions can be constructed from a time series of excitation energies computed for configurations along a molecular dynamics (MD) trajectory, usually obtained from ground-state dynamics that sample the region of vertical excitation.<sup>55,56</sup> MD trajectories generally treat the nuclei classically and thus produce classical correlation functions, but the necessary quantum correlation functions can be approximated with a quantum correction factor.<sup>57–60</sup> Although the cumulant expansion of the LR function is formally exact, in practice it is generally truncated at second or third order. Truncation at second order is exact for a system with a Gaussian distribution of energy gap fluctuations, which occurs for displaced harmonic potentials of the same frequency. Changing the frequency or rotating the potentials may introduce nonlinear coupling that can be partially captured by the third-order term, which is also able to incorporate some effects of anharmonic potentials.<sup>55,61</sup> In addition to being able to sample anharmonic nuclear configurations, a dynamic MD energy gap time-correlation function-based approach also describes coupling to an explicit solvent environment.<sup>55,56,61–63</sup>

In this work, we compare the abovementioned methods for modeling the excited states and linear absorption vibronic spectrum of the methylene blue chromophore in vacuum. A recent study by de Queiroz et al. of the  $S_0 \rightarrow S_1$  Franck–Condon vibronic spectrum in vacuo, obtained at the LR-TDDFT B3LYP/def2-SV(P) level of theory, predicts a very large vibronic shoulder.<sup>64</sup> However, very recent work by some of the authors of this paper suggests that the LR-TD-B3LYP  $S_0 \rightarrow S_1$  vibronic shoulder may be due to  $S_1/S_2$  state mixing and a potential breakdown of the Born–Oppenheimer approximation.<sup>65</sup> Such state mixing and a breakdown of the Born–Oppenheimer approximation requires inclusion of nonadiabatic effects to account for coupling between states and population transfer between the  $S_1$  and  $S_2$  state; the standard approaches for modeling vibronic spectra mentioned above therefore likely cannot be accurately applied to methylene blue. However, this state mixing presents an opportunity to showcase the differences in methods, highlights the ability of the PIMOM approach as a viable method for both the generation of approximately diabatic surfaces and affordable excited-state forces, and introduces alternative diagnostics to indicate the breakdown of the Born–Oppenheimer approximation in spectral simulations. After giving a brief overview of the PIMOM and various methods for computing absorption spectra, we compare excited states computed with adiabatic LR-TDDFT and PIMOM for methylene blue. We then showcase the simulated vibronic spectra computed with the following approaches: adiabatic Hessian LR-TDDFT, vertical gradient LR-TDDFT, Hessian PIMOM, and a truncated cumulant expansion of the LR function obtained from computed energy gaps along an MD trajectory. Computation of the spectral densities reveals which normal mode couples most strongly to the optical excitation and is responsible for the large vibronic shoulder predicted by adiabatic Hessian LR-TD-B3LYP. The analysis of the  $B_2$  normal mode at  $1494\text{ cm}^{-1}$  shows that LR-TD-B3LYP predicts  $S_1/S_2$  state mixing along this coordinate. In contrast, the PIMOM predicts an  $S_1$  PES of consistent character and produces a vibronic spectrum accordant with vertical gradient and MD trajectory approaches.

## 2. THEORETICAL BACKGROUND

**2.1. Self-Consistent Field with the PIMOM.** The  $\Delta$ SCF approach for studying electronic excited states proceeds by optimization to an SCF solution that represents a singly or multiply excited state. This approach is generally much simpler than alternatives such as those based on modified variational schemes or those introducing user-defined constraints. The primary challenge to the straightforward use of SCF programs for excited states is that those solutions necessarily correspond to non-aufbau results. The resulting SCF solutions will either be a local minimum (typically not the global minimum) or a saddle point.<sup>66</sup> Without altering standard SCF optimizers, calculations targeting excited electronic states often result in so-called “variational collapse”, where the target state is lost and the SCF procedure converges to the ground state. One family of techniques that has shown great success in overcoming variational collapse is the maximum overlap methods (MOMs).<sup>18,66,67</sup> Recently, the Pribram-Jones and Hratchian groups explored the behavior of a particular MOM scheme labeled the PIMOM.<sup>16</sup>

MOMs alter standard SCF optimizers to drive convergence toward an alternative (typically) non-aufbau result. MOMs aim the SCF procedure at a user-defined target by choosing occupied MOs based on those with the largest agreement with the target determinant’s occupied subspace rather than on their one-electron orbital energies. Different MOMs use varying metrics for determining such non-aufbau occupations. In the case of the PIMOM, occupied/virtual permutations are employed at each SCF cycle based on the projection of each current MO onto the target system’s occupied MO space. Mathematically, the PIMOM relies on a density projection operator,  $\mathcal{P}^{\text{target}}$ , to define a modified aufbau metric according to

$$\mathcal{P}^{\text{target}} = \sum_i |i^{\text{target}}\rangle\langle i^{\text{target}}| \quad (1)$$

This projection operator in the current MO basis at each SCF cycle is

$$P_{pq}^{\text{target}} = \langle p | \mathcal{P}^{\text{target}} | q \rangle = \sum_i \langle p | i^{\text{target}} \rangle \langle i^{\text{target}} | q \rangle \quad (2)$$

where  $|i^{\text{target}}\rangle$  is the initial set of MOs,  $|p\rangle$  and  $|q\rangle$  are the current sets of MOs.

Equation 2 can be further decomposed to

$$P_{pq}^{\text{target}} = \sum_i \sum_{\mu\nu} \sum_{\lambda\sigma} C_{\mu p} S_{\mu\lambda} C_{\lambda i}^{\text{target}} C_{\sigma i}^{\text{target}} S_{\sigma\nu} C_{\nu q} \quad (3)$$

where  $\mathbf{C}$  and  $\mathbf{C}^{\text{target}}$  are the current and target sets of MO coefficients, respectively.  $\mathbf{S}$  is the atomic orbital overlap matrix.

Given that the MO basis is orthonormal,  $P_{pq}^{\text{target}}$  can be used to give the target density’s gross Mulliken populations partitioned into the current MO basis. With this in mind, the PIMOM model defines a modified aufbau metric,  $s_p$ , as

$$s_p = \sum_q P_{pq}^{\text{target}} \quad (4)$$

Thus, the MOs with the largest  $s_p$  are chosen to be occupied.

The use of SCF representations for excited states introduces some limitations. For example, the SCF excited-state wave function solution is not necessarily orthogonal to the ground-state wave function, which can impact properties such as transition dipoles and oscillator strengths. However, in many applications reported using this approach, the wave functions

are, in fact, orthogonal or very nearly orthogonal, and potential nonorthogonality effects are either avoided or minimal. Additionally, many SCF excited states will result in spontaneous (spin) symmetry breaking due to the single-determinant nature of the SCF model. Often, errors due to such a situation can be adequately addressed using approximate projection techniques.<sup>17,23,68–71</sup>

On the other hand, using a method such as the PIMOM when studying excited states has significant advantages. Notably, the PIMOM (and other MOM schemes) work within standard and readily available ground-state machinery, including highly efficient programs for evaluating analytic derivatives and properties. This leads to computational expenses that are the same as for a standard ground-state Hartree-Fock or DFT calculation. The MOM family of methods is also able to model challenging excited states, including double excitations.<sup>66</sup> Additionally, recent work suggests that  $\Delta$ SCF approaches may yield states exhibiting consistent charge or spin character across the PES and, under some situations, may provide a route to generating diabatic states.<sup>72</sup> Other recent studies suggest that MOM may be able to produce both diabatic and adiabatic states in the regions of surface crossings, with the nature of the state depending on the nature of the SCF solution and its orbital rotation Hessian.<sup>24,29</sup>

Note that electronic relaxation is accounted for in SCF calculations of excited states due to changes in the mean-field potential included in the Fock operator (relative to the ground state) resulting from changes in occupied MOs. This relaxation is different than that captured by LR-TDDFT, and thus we expect the excitation energies to be different as well. Related effects have been studied in detail in the context of ionization potential and electron affinity calculations.<sup>73</sup>

**2.2. Computing Optical Spectra.** In this subsection, we outline two main approaches for computing linear vibronic absorption spectra. The first approach computes the LR function directly from the harmonic wave functions as determined from the normal modes that parametrize a GBOM. As the wave functions of the ground and excited states are directly computed, such an approach is exact within the harmonic Franck–Condon principle. The second approach approximates the LR function based on a truncated cumulant expansion, in which each term in the cumulant expansion can be determined from the computation of an energy gap time-correlation function. The energy gap time-correlation functions can be determined exactly for a GBOM and can also be computed directly from an MD trajectory, both of which we utilize in this study.

**2.2.1. Linear Absorption Vibronic Spectra in the Harmonic Franck–Condon Hessian or Vertical Gradient Approach.** The GBOM consists of harmonic potentials of differing frequencies that may be rotated with respect to each other. In the GBOM, the nuclear Hamiltonians for the electronic ground and excited states with  $N_j$  vibrational modes can be written as

$$H_g(\hat{\mathbf{q}}_g, \hat{\mathbf{p}}_g) = \frac{1}{2} \sum_j^{N_j} [\hat{p}_{g,j}^2 + \omega_{g,j}^2 \hat{q}_{g,j}^2] \quad (\text{Sa})$$

$$H_e(\hat{\mathbf{q}}_e, \hat{\mathbf{p}}_e) = \frac{1}{2} \sum_j^{N_j} [\hat{p}_{e,j}^2 + \omega_{e,j}^2 \hat{q}_{e,j}^2] + \Delta_{eg}^0 \quad (\text{Sb})$$



where  $\Delta_{\text{eg}}^0$  is the energy gap between the ground- and excited-state minima, and the ground- and excited-state normal modes are related through the linear transformation

$$\hat{q}_{g,i} = \sum_j^{N_j} J_{ij} \hat{q}_{e,j} + K_i \quad (6)$$

here,  $\mathbf{K}$  is the shift vector describing the displacement between ground- and excited-state PES minima, and  $\mathbf{J}$  is the Duschinsky rotation matrix. Both the difference in curvature, with  $\omega_{g,i} \neq \omega_{e,i}$ , and the Duschinsky rotation lead to non-Gaussian energy gap fluctuations.<sup>55</sup>

Computing the harmonic normal modes at the ground- and excited-state-optimized geometries and the corresponding wave functions, displacements, and a Duschinsky rotation allows exact computation of the absorption vibronic spectrum for a GBOM within the Franck–Condon approach, wherein overlaps between ground- and excited-state harmonic oscillator wave functions determine the intensity of vibronic peaks in the spectrum

$$\sigma_{\text{FC}}(\omega) \propto \omega |V_{\text{ge}}|^2 \sum_{\nu_g} \rho(\nu_g) \sum_{\nu_e} |\langle \phi_{\nu_g} | \phi_{\nu_e} \rangle|^2 \times \mathcal{N}(\omega - [\omega_{\nu_e} - \omega_{\nu_g}], s) \quad (7)$$

Here,  $V_{\text{ge}}$  is the transition dipole between the ground and excited electronic states,  $|\phi_{\nu_g}\rangle$  and  $|\phi_{\nu_e}\rangle$  denote nuclear wave functions, and  $\omega_{\nu_g}$  and  $\omega_{\nu_e}$  represent the corresponding total energy of the system in the ground and excited states, respectively. The Boltzmann population  $\rho(\nu_g)$  determines the occupation of the ground-state vibrational levels at a given temperature. The Franck–Condon overlap integral  $\langle \phi_{\nu_g} | \phi_{\nu_e} \rangle$  gives the intensity of the vibronic transitions between different vibrational levels. Transitions are broadened by a Gaussian function  $\mathcal{N}(\omega - [\omega_{\nu_e} - \omega_{\nu_g}], s)$ , where the broadening parameter  $s$  is chosen either in an ad hoc manner or can be estimated from first principles according to Marcus theory.<sup>74</sup> This harmonic Franck–Condon approach can be implemented using time-dependent (effective for large multimode systems and finite temperature calculations) and time-independent (sum over states, effective for smaller systems or zero temperature calculations) techniques, with extension to Herzberg–Teller effects that include linear effects of the structure on transition dipole moments.<sup>43,45,75–77</sup>

The Franck–Condon absorption spectra can also be computed within a vertical gradient approximation,<sup>49,50,77</sup> which avoids the geometry optimization of the electronic excited state and instead computes the excited-state gradient at the ground-state-optimized geometry in order to approximate the location of the excited-state minimum.<sup>77</sup> The curvature of the excited-state potential, and therefore normal modes and frequencies, are assumed to be the same as in the ground state.

**2.2.2. Linear Absorption Vibronic Spectra in the Cumulant Approach.** For a two-level electronic system consisting of an electronic ground state and a single-electronic excited state coupled to nuclear motion and within the Condon approximation, it is possible to write the linear absorption vibronic spectrum in terms of a cumulant expansion of the energy gap fluctuation operator  $\delta U = H_e - H_g - \omega_{\text{eg}}^{\text{av}} = U - \omega_{\text{eg}}^{\text{av}}$ <sup>54</sup>

$$\begin{aligned} \sigma(\omega) &\propto \omega |V_{\text{ge}}|^2 \text{Re} \int_0^\infty dt e^{i(\omega - \omega_{\text{eg}}^{\text{av}})t} \\ &\quad \times \langle \exp_+ [-i \int_0^t d\tau \delta U[\hat{q}(\tau)]] \rangle \\ &\propto \omega |V_{\text{ge}}|^2 \text{Re} \int_0^\infty dt e^{i(\omega - \omega_{\text{eg}}^{\text{av}})t} \exp \left[ \sum_{n=2}^\infty g_n(t) \right] \end{aligned} \quad (8)$$

Here,  $\omega_{\text{eg}}^{\text{av}} = \langle U(\hat{q}) \rangle$  is the thermal average of the energy gap operator,  $g_n(t)$  is the  $n^{\text{th}}$  order cumulant, and Hartree atomic units are used throughout. We re-express the response function as an infinite expansion with respect to cumulants (combinations of moments) of the energy gap fluctuation, rewriting the time-ordered exponentiated integral (denoted by  $\exp_+$ ) of the energy gap operator as the exponentiated sum of cumulants, and then match terms order by order in  $\delta U$ . If the energy gap fluctuations are Gaussian, as is true for the quadratic potential of a simple displaced harmonic oscillator system where ground- and excited-state energy surfaces have the same curvature, the cumulant expansion in eq 7 can be exactly truncated at second order.<sup>54</sup> For more realistic PESs, or if the frequencies of the two potentials are different or rotated with respect to each other, higher order cumulants will contribute to the lineshape.<sup>55,78</sup> The cumulants can be expressed in terms of time-ordered integrals of increasing orders of quantum time-correlation functions  $C_{\delta U}$  of the energy gap fluctuation operator  $\delta U$ . For the second-order cumulant, we can write

$$g_2(t) = \int_0^t d\tau_2 \int_0^{\tau_2} d\tau_1 C_{\delta U}^{(2)}(\tau_2 - \tau_1) \quad (9)$$

where

$$C_{\delta U}^{(2)}(t) = \langle \delta U(t) \delta U(0) \rangle \quad (10)$$

with analogous expressions for higher order quantum correlation functions.<sup>8</sup>

The second-order cumulant contribution  $g_2(t)$  can be written in terms of the spectral density  $\mathcal{J}(\omega)$  by switching into Fourier space<sup>54</sup>

$$\begin{aligned} g_2(t) &= \frac{1}{\pi} \int_0^\infty d\omega \frac{\mathcal{J}(\omega)}{\omega^2} \left[ \coth\left(\frac{\beta\omega}{2}\right) [1 - \cos(\omega t)] \right. \\ &\quad \left. - i[\sin(\omega t) - \omega t] \right] \end{aligned} \quad (11)$$

with  $\beta = 1/(k_B T)$  and

$$\mathcal{J}(\omega) = i\theta(\omega) \int dt e^{i\omega t} \text{Im} C_{\delta U}^{(2)}(t) \quad (12)$$

a similar expression can be derived for the third-order correction  $g_3(t)$ .<sup>55</sup> As we have recently demonstrated,<sup>55</sup> the third-order cumulant correction can provide improvements in the absorption lineshapes of systems with moderately anharmonic potentials. The exact quantum correlation function  $C_{\delta U}(t)$  is in general impossible to compute except for simple model systems. In previous work, some of the authors derived and implemented the exact quantum time-correlation functions needed for the second-order and third-order cumulant terms for the GBOM, including Duschinsky rotation effects,<sup>55</sup> which we make use of in this work. For a more realistic system,  $C_{\delta U}(t)$  can be computed from an MD trajectory, where it is approximately reconstructed from its classical counterpart,  $C_c(t)$  using quantum correction factors.<sup>57–59</sup> In this work, for the spectra built from correlation

functions produced from an MD trajectory, we use the harmonic quantum correction factor,<sup>58,60</sup> yielding

$$\mathcal{F}(\omega) \approx \theta(\omega) \frac{\beta\omega}{2} \int dt e^{i\omega t} C_{cl}^{(2)}(t) \quad (13)$$

where  $\beta = 1/k_B T$  and  $\theta(\omega)$  is the Heaviside step function.

This cumulant expansion method expands the dipole response function for a two-level system, allowing the use of MD-based energy gap correlation functions instead of nuclear wave functions in the response function. In the previous study of methylene blue in solution by some of the authors, we made use of these MD-derived correlation functions and spectral densities to parametrize a linear vibronic coupling Hamiltonian for three states while directly capturing solvent coupling to chromophore motion.<sup>65</sup> The linear vibronic coupling Hamiltonian often employs the highly accurate but very expensive multiconfigurational time-dependent Hartree approach,<sup>79</sup> but in our recent study of methylene blue we used a matrix product states/tensor network ansatz<sup>80</sup> with the spectral densities employing the second-order cumulant expansion to describe the system–bath coupling between electronic states.

### 3. COMPUTATIONAL DETAILS

**3.1. Geometry Optimization, Normal Mode Computation, and Franck–Condon Vibronic Spectral Calculations.** All ground- and excited-state structures were optimized using the hybrid B3LYP and the range-separated hybrid CAM-B3LYP functionals with the 6-31+G\* Pople basis set,<sup>81</sup> with ground-state Kohn–Sham determinants tested for stability.<sup>82,83</sup> Excited-state calculations were carried out using the same model chemistry either within the LR formalism<sup>8,84,85</sup> or with the PIMOM  $\Delta$ SCF method. Initial guesses, which serve as target determinants, for PIMOM  $\Delta$ SCF calculations were generated by permuting ground-state MOs to resemble the desired excited state. The highest occupied molecular orbital–lowest unoccupied molecular orbital (HOMO–LUMO) MOs were permuted to generate the  $S_1$  initial guess, while HOMO-1 to LUMO MOs were permuted for calculations of the  $S_2$  state. All the  $\Delta$ SCF results were obtained using an implementation of the PIMOM algorithm in a local development version of Gaussian.<sup>86</sup> The analyses for converged electronic excited states were facilitated by using a modified form of the natural ionization orbital (NIO) model by Hratchian and co-workers.<sup>87–89</sup> Using the NIO model, converged electronic excited states were verified by visualizing the natural orbitals of the difference densities relative to the ground state. This scheme is analogous to the natural transition orbital model of Martin,<sup>90</sup> but directly separates electron–hole pairs from orbital relaxation contributions in the difference density from a  $\Delta$ SCF set of calculations.

We note that one inherent challenge with the  $\Delta$ SCF approach to studies of one-electron excited states is that such SCF solutions often exhibit spin symmetry breaking, which can be observed as spin contamination. Spin contamination results when a single-determinant SCF solution is not an eigenstate of the  $S^2$  operator and can be described as resulting from an admixture of a desired pure spin state and *contaminating* higher spin states.<sup>91</sup> Preliminary calculations following protocols developed in one of our laboratories and considering approximate (spin) projection models to remedy impacted energies, forces, and force constants suggested that spin contamination should not negatively impact the PIMOM-based spectral simulations reported in this study.<sup>68–71,92–95</sup>

Molecular geometries for ground and excited states were optimized using standard methods,<sup>96</sup> and the reported PES minima were verified using analytical second-derivative calculations.<sup>97,98</sup> The methylene blue ground-state  $S_0$ -optimized structure is of  $C_{2v}$  symmetry for both B3LYP and CAM-B3LYP. This  $C_{2v}$  symmetry is maintained for the  $S_1$  minimum obtained for PIMOM/B3LYP, PIMOM/CAM-B3LYP, and LR-TDDFT/CAM-B3LYP. However, for the LR-TDDFT/B3LYP, the  $S_1$  minimum is of  $C_s$  symmetry.

Hessian-based vibronic spectra, under the harmonic approximation, were simulated using the implementation by Bloino, Barone, and co-workers for both the PIMOM and LR-TDDFT by computing the Hessian and displacements at the ground- and excited-state minima.<sup>99</sup> The vertical gradient Franck–Condon vibronic spectra for LR-TDDFT were also computed.<sup>49,50,77</sup> All the spectra are scaled so that the  $\lambda_{max}$  intensities are unity.

**3.2. Parametrization of Generalized Brownian Oscillator Model.** We used the ground- and excited-state geometry optimizations and normal modes from the LR-TDDFT and PIMOM calculations to construct the GBOM for methylene blue. The Franck–Condon spectrum provides the exact solution to the LR spectrum of the GBOM. The shift vector  $\mathbf{K}$  and the Duschinsky rotation matrix  $\mathbf{J}$  were computed with Gaussian. The parametrized GBOM was used to construct the spectral density and the truncated cumulant expansion-based linear absorption spectra. For the parametrized GBOM that includes Duschinsky rotation effects, we use our previously implemented analytical expressions for the exact quantum time-correlation functions needed for the second-order and third-order cumulant terms<sup>55</sup> within the open-source MolSpeckPy package<sup>100</sup> developed by the Isborn and Zuehlsdorff groups.

**3.3. Ab Initio Molecular Dynamics, Computation of Vertical Excitation Energies, and Energy Gap Correlation Functions.** We performed ab initio MD (AIMD) simulations of methylene blue in vacuum in the NVT ensemble at  $T = 300$  K. The AIMD simulations employed a 0.5 fs time step for a 17 ps run. Two sets of AIMD calculations were carried out at the same level of theory as the ground-state geometry optimizations, employing both B3LYP and CAM-B3LYP with the 6-31+G\* basis set. To compute the correlation functions needed for the linear absorption spectroscopy, we discarded the first 1 ps for equilibration from AIMD trajectories and then extracted the snapshots every 2 fs from the last 16 ps of each trajectory, yielding a total of 8000 snapshots for energy gap calculations. For each snapshot, LR-TDDFT excited-state calculations were performed at the corresponding level of theory.

Upon analyzing the  $S_1$  and  $S_2$  LR-TDDFT states along the AIMD trajectory, we find substantial excited state reordering and mixing for the LR-TD-B3LYP states, confirming the need for a nonadiabatic treatment of the spectra as we applied in previous work.<sup>65</sup> The LR-TD-CAM-B3LYP states do not mix during the trajectory. The cumulant-based approach employed here assumes a two-state model, and thus does not account for mixing between states. We therefore use the quasi-diabatization strategy outlined by Subotnik and co-workers,<sup>101</sup> where the transition dipole matrix  $\mathbf{D}$  is defined as

$$\mathbf{D} = \begin{pmatrix} V_{01} \cdot V_{01} & V_{01} \cdot V_{02} \\ V_{01} \cdot V_{02} & V_{02} \cdot V_{02} \end{pmatrix} \quad (14)$$

where  $V_{0n}$  is the transition dipole moment between the ground state and state  $n$ . Diagonalizing  $\mathbf{D}$  produces two states with maximally different transition dipole moments, where the

**Table 1.** For Methylene Blue in Vacuum, B3LYP  $S_2 - S_1$  Electronic Energy Gaps in eV at  $S_0$ ,  $S_1^{\text{LR-TDDFT}}$ , and  $S_1^{\text{PIMOM}}$  Optimized Geometries Obtained Using PIMOM and LR-TDDFT Approaches<sup>a</sup>

optimized geometry	PIMOM		LR-TDDFT	
	$E_{S_2} - E_{S_1}$ (eV)	$f_{S_1}/f_{S_2}$	$E_{S_2} - E_{S_1}$ (eV)	$f_{S_1}/f_{S_2}$
$S_0$	0.54	0.662/0.006	0.13	0.810/0.001
$S_1^{\text{LR-TDDFT}}$	0.44	0.571/0.046	0.29	0.382/0.350
$S_1^{\text{PIMOM}}$	0.52	0.621/0.004	0.10	0.796/0.003

<sup>a</sup>Oscillator strengths ( $f$ ) of  $S_1$  and  $S_2$  are also reported and separated by “/”.

**Table 2.** For Methylene Blue in Vacuum, CAM-B3LYP  $S_2 - S_1$  Electronic Energy Gaps in eV at  $S_0$ ,  $S_1^{\text{PIMOM}}$ , and  $S_1^{\text{LR-TDDFT}}$  Optimized Geometries Obtained Using PIMOM and LR-TDDFT Approaches<sup>a</sup>

optimized geometry	PIMOM		LR-TDDFT	
	$E_{S_2} - E_{S_1}$ (eV)	$f_{S_1}/f_{S_2}$	$E_{S_2} - E_{S_1}$ (eV)	$f_{S_1}/f_{S_2}$
$S_0$	0.49	0.615/0.014	0.38	0.959/0.006
$S_1^{\text{LR-TDDFT}}$	0.47	0.517/0.011	0.36	0.930/0.006
$S_1^{\text{PIMOM}}$	0.47	0.692/0.011	0.34	0.931/0.006

<sup>a</sup>Oscillator strengths of  $S_1$  and  $S_2$  are also reported and separated by “/”.

eigenvectors are then used to rotate the diagonal matrix of adiabatic excitation energies into a matrix with two diabatic excitation energies on the diagonal and their electronic coupling as the off-diagonal elements. We performed this  $S_1$  and  $S_2$  diabaticization for every snapshot along the AIMD trajectory, then used the resulting energy gaps to construct the classical autocorrelation function  $C_{cl}(t)$  used to determine the spectral density and AIMD-based cumulant lineshapes. The quasi-diabatization procedure is also used for the analysis of  $S_1$  and  $S_2$  with the normal mode analysis.

Further details of the formalism and implementation of spectral densities and cumulant lineshape calculations based upon  $C_{cl}(t)$  can be found in recent publications by some of the authors, and are available in the MolSpeckPy package.<sup>100</sup>

## 4. RESULTS AND DISCUSSION

### 4.1. Comparison of PIMOM and LR-TDDFT Excitation Energies and Difference Densities.

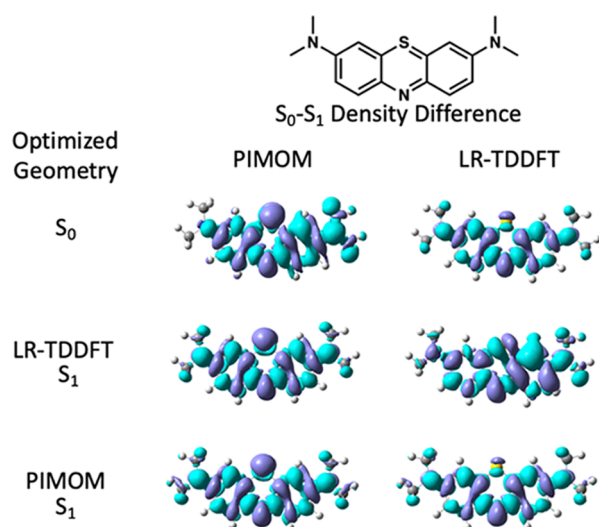
Before analyzing vibronic absorption spectra for methylene blue computed with different methods, it is worthwhile to examine the excitation energies computed with the PIMOM and LR-TDDFT for the vertical excitation energies computed at the  $S_0$  ground-state-optimized geometry and at the  $S_1$  excited-state-optimized geometry. At the  $S_0$  minimum, the  $S_1$  state is primarily HOMO  $\rightarrow$  LUMO character, whereas the  $S_2$  state is primarily HOMO-1  $\rightarrow$  LUMO character. These MO occupations were used to find the corresponding PIMOM excited states and corresponding excited-state-optimized structures. As has recently been shown for the PIMOM,<sup>16,17</sup> the excitation energies from the ground state to the excited state are significantly lower than those predicted with LR-TDDFT. For methylene blue, the PIMOM energies are 0.8–0.9 eV lower than the LR-TDDFT energies, see the Supporting Information. Although the PIMOM predicts overly low excitation energies due to the additional relaxation of the excited state in the SCF process, excited-state properties such as vibrational frequency are more accurately modeled with the PIMOM compared to LR-TDDFT,<sup>17</sup> and the PIMOM treats excited states on equal footing, suggesting that it will produce a more reliable gap between excited states. Here, in the main manuscript, we focus on the energy differences between  $S_1$  and  $S_2$  excited states of methylene blue in vacuum.

Table 1 shows the oscillator strengths and energy gaps between the  $S_1$  and  $S_2$  states computed with the PIMOM and LR-TD-B3LYP for the  $S_0$  minimum and for the excited-state  $S_1$  minimum for both methods. The PIMOM  $S_1$  minimum retains the  $C_{2v}$  symmetry of the ground state, but the LR-TD-B3LYP  $S_1$  minimum has  $C_s$  symmetry. At all the geometries, the energy gaps between the  $S_1$  and  $S_2$  states are larger for the PIMOM than for LR-TDDFT, with LR-TD-B3LYP having a fairly small energy gap of 0.1–0.3 eV. Interestingly, at the LR-TD-B3LYP  $S_1$  minimum, the energy gap decreases for the PIMOM and increases for LR-TD-B3LYP. At this LR-TD-B3LYP  $S_1$ -optimized geometry, the LR oscillator strength  $f$  of both the  $S_0 \rightarrow S_1$  and the  $S_0 \rightarrow S_2$  changes substantially, with the bright  $S_1$  transition losing oscillator strength and the dark  $S_2$  transition gaining oscillator strength, suggesting that the  $S_1/S_2$  state mixing is the cause of the reduced symmetry of the LR-TD-B3LYP  $S_1$  minimum. At this geometry, the LR states indicate substantial mixing due to nearly equal values of their oscillator strengths. This mixing is supported by the MO contributions, which at this geometry are a mixture of HOMO  $\rightarrow$  LUMO and HOMO-1  $\rightarrow$  LUMO.

In contrast to LR-TD-B3LYP, LR-TD-CAM-B3LYP yields  $S_1$  and  $S_2$  states that retain the same character for the geometries considered here, with similar  $S_1$  to  $S_2$  energy gaps and oscillator strengths for  $S_0$  and both  $S_1$  geometries, see Table 2. The LR-TD-CAM-B3LYP energy gap between  $S_1$  and  $S_2$  is also larger than that with LR-TD-B3LYP, which would lead to less state mixing. The difference between TD-B3LYP and TD-CAM-B3LYP points to TDDFT's unequal treatment of states with differing degrees of charge-transfer character. The PIMOM shows the  $S_1$  to  $S_2$  CAM-B3LYP gap being a bit smaller than the B3LYP gap. Unlike LR-TDDFT, the PIMOM shows consistent results with both functionals, with both the PIMOM B3LYP and CAM-B3LYP  $S_1$  to  $S_2$  energy gap decreasing by 0.02 eV going from the  $S_0$  minimum to the PIMOM  $S_1$  minimum.

To further illustrate the behavioral difference between LR-TDDFT and PIMOM, the B3LYP electron density differences between the ground- and  $S_1$  excited-state densities computed at the LR-TDDFT  $S_1$ , PIMOM  $S_1$ , and ground-state-optimized geometries are shown in Figure 1. The PIMOM produces a consistent density difference for all the three optimized geometries, indicating that the character of the  $S_1$  state remains





**Figure 1.** Structure of the methylene blue chromophore and the B3LYP density difference between the ground and  $S_1$  excited state at the ground-state  $S_0$ , LR-TDDFT  $S_1$ , and PIMOM  $S_1$  optimized geometries.

the same for all three geometries. The LR-TD-B3LYP density differences obtained at the ground state and the PIMOM-optimized geometries are similar to the density differences predicted by the PIMOM. In contrast, at the LR-TD-B3LYP  $S_1$  minimum, the LR-TD-B3LYP difference density shows qualitatively different characters, with notable symmetry breaking, demonstrating that the PIMOM and LR-TDDFT produce  $S_1$  states of substantially different character for this geometry. The CAM-B3LYP density differences (shown in the Supporting Information, Figure S1) are in excellent agreement for both the PIMOM and LR-TDDFT for all geometries. The CAM-B3LYP PIMOM density differences are very similar to the B3LYP PIMOM density differences, showing that the PIMOM produces excited states of similar character for both functionals.

**4.2. Linear Absorption Spectra.** Although nonadiabatic methods that account for population transfer between the  $S_1$  and  $S_2$  surfaces should be used to accurately model the spectrum of methylene blue,<sup>65</sup> we here compare the spectra computed with only consideration of a vertical transition from the ground state to the  $S_1$  excited state. These methods ignore nonadiabatic effects, but this comparison highlights differences between methods and offers a new diagnostic for when nonadiabatic effects should be considered. The four spectral methods, which

consist of the adiabatic Hessian LR-TDDFT, vertical gradient LR-TDDFT, Hessian-based PIMOM, and AIMD, are compared in Figure 2 for B3LYP and CAM-B3LYP. The vibronic spectra for (PIMOM and AIMD) are shifted by (0.83 and  $-0.05$  eV) for B3LYP and (0.76 and  $-0.03$  eV) for CAM-B3LYP, respectively. These shifts align the energy of the 0–0 transition, allowing a better comparison of the lineshape.

Each of the methods examined here employs different approximations. LR-TDDFT is an adiabatic, perturbative approach. Additionally, the adiabatic Hessian and harmonic approximations at the LR-TDDFT excited-state minimum may not be appropriate if PESs mix together in this region, as the curvature is likely very anharmonic in the regions of adiabatic state mixing. In contrast, the vertical gradient approach avoids the computation of the excited-state minimum and normal modes, instead computing only the excited-state gradient at the optimized geometry of the ground state.

In Figure 2a, we see significant differences in the spectra computed with the adiabatic Hessian LR-TD-B3LYP approach, obtained with full geometry optimization and normal mode computation at the LR  $S_1$  minimum, compared to that obtained with the vertical gradient approach. Note that both of these LR methods use the same ground-state normal modes. Thus, the only difference is the treatment of the  $S_1$  excited-state surface, suggesting that the character of the LR-TD-B3LYP PES is very different in the region above the  $S_0$  minimum compared to the PES in the region of the  $S_1$  minimum. This result is consistent with the results of the previous section that found a substantial change in the LR-TDDFT electron density difference at the  $S_1$  minimum compared to the  $S_0$  minimum. The vibronic spectrum obtained within the vertical gradient approach is much narrower due to the small vibronic shoulder peak; this same peak is almost as large as the 0–0 transition for the adiabatic Hessian approach, showing that the  $S_1$  minimum likely undergoes a significant change in geometry. The spectral discrepancy is consistent with the results of Avila Ferrer and Santoro that showed that discrepancies in the vibronic spectra of vertical gradient and adiabatic Hessian approaches can be used as a diagnostic for the failure of the Born–Oppenheimer or harmonic approximations resulting from state mixing.<sup>53</sup>

The LR-TD-B3LYP vibronic spectrum obtained within the vertical gradient approach shows good agreement with the AIMD trajectory-based approach that employs second-order truncation of the cumulant expansion. This latter method may sample nuclear configurations that may occur in anharmonic

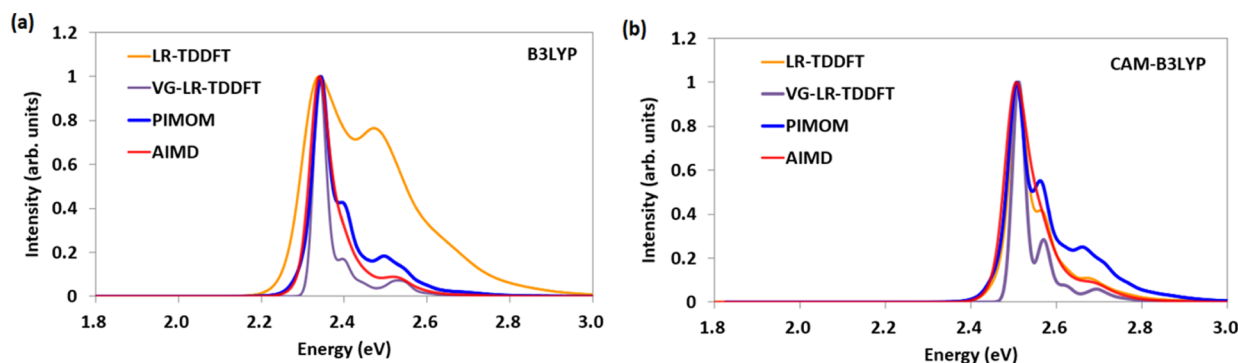


**Figure 2.** (a) B3LYP and (b) CAM-B3LYP  $S_0 \rightarrow S_1$  vibronic spectra computed with: the adiabatic Hessian from LR-TDDFT, the vertical gradient from LR-TDDFT (VG-LR-TDDFT), the Hessian from the PIMOM, and LR-TDDFT energy gap time-correlation function from the ground-state AIMD trajectory (AIMD). Note that spectra are energetically aligned as mentioned in the main text.

regions of the potential, which could be responsible for the increased broadening compared to the vertical gradient approach. The good agreement between the methods is perhaps not surprising because both methods are sampling the  $S_1$  PES above the  $S_0$  minimum. Interestingly, if the same LR-TDDFT  $S_1$  normal modes and displacements that characterize the vibronic spectrum are used to compute the spectrum within the second- or third-order truncation to the cumulant expansion of the LR function within the GBOM, large changes between the spectra generated with the second and third cumulant truncation suggest significant changes in the curvature of the ground- and excited-state PES and/or a large Duschinsky rotation, leading to non-Gaussian fluctuations of the energy gap (see Supporting Information, Figures S2–S4). These large differences in curvature or a large rotation of normal modes may be due to the symmetry breaking going from the ground-state  $S_0$  minimum to the LR-TD-B3LYP  $S_1$  minimum.

Perhaps the most striking result of this work is the comparison of the spectra computed with the Hessian and normal modes of the  $\Delta$ SCF B3LYP PIMOM  $S_1$  minimum to that computed from the LR-TD-B3LYP  $S_1$  minimum, see Figure 2a, where we again see a large difference between the intensity of the vibronic shoulder peak. The spectrum obtained with the PIMOM  $S_1$  minimum normal modes is in good agreement with both the vertical gradient and the AIMD trajectory-based methods, suggesting that all three of these methods are consistent in their treatment of the character of the  $S_1$  state. In Figure 2b, the same spectra are compared for computation with the CAM-B3LYP functional. Here, we see much better agreement with all the methods. The adiabatic Hessian LR-TD-CAM-B3LYP and AIMD-based spectra computed from the LR-TD-CAM-B3LYP excitation energies are nearly indistinguishable. The CAM-B3LYP functional predicts a larger gap between the  $S_1$  and  $S_2$  states, suggesting that there is much less mixing of these two excited states and, as seen from the excitation energies and oscillator strengths, the LR-TD-CAM-B3LYP  $S_1$  state maintains similar character in the region of the vertical transition and at both the LR and PIMOM  $S_1$  minima.

Plotting the spectral density, eqs 11 and 12, allows us to compare how the different methods treat the modes that couple the  $S_0$  and  $S_1$  transitions. The spectral densities in Figure 3 computed from the LR-TDDFT and PIMOM are both obtained from a GBOM parametrized with the ground- and excited-state normal modes. We also show the spectral density computed from the energy gap time-correlation function obtained from the AIMD trajectory. The spectral density based on the AIMD

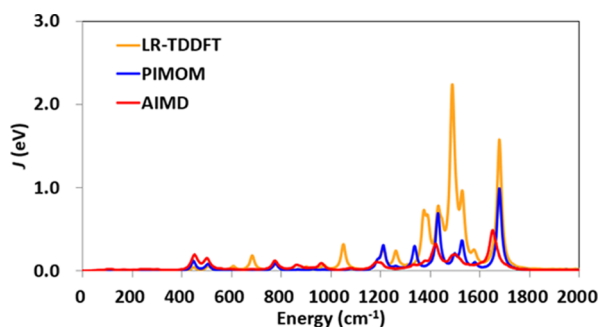


**Figure 3.** B3LYP  $S_0/S_1$  spectral density computed using parameters from the LR-TDDFT and PIMOM normal modes from  $S_0$  and  $S_1$  optimized geometries, and that computed from the  $S_0$  to  $S_1$  energy gap time-correlation function along the ground-state AIMD trajectory.

trajectory shows  $\sim 10$ – $20$   $\text{cm}^{-1}$  red-shift of the peaks compared with the normal mode parametrization due to the inclusion of anharmonicity of the PES in the vibrations of the chromophore. The spectral densities in Figure 3 show that there is a high-intensity peak at around  $1500$   $\text{cm}^{-1}$  in the LR-TDDFT spectral density, whereas the same region of the PIMOM and AIMD trajectory spectral density shows very little intensity. This large peak, corresponding to a normal mode of  $B_2$  symmetry, is responsible for the significant vibronic shoulder present in the adiabatic Hessian LR-TDDFT spectrum. This ground-state normal mode involves antisymmetric C–C stretches of the center ring coupled to the motion of the dimethylamine groups. The LR-TD-B3LYP  $S_1$  minimum is not of  $C_{2v}$  symmetry and the symmetry reduction to  $C_s$  symmetry leads to enhanced coupling with the antisymmetric stretch, giving rise to the large peak in spectral density. We further analyze this normal mode in the following section.

**4.3. Normal Mode Analysis.** To analyze the nature of the  $S_1$  and  $S_2$  PESs along the  $B_2$  antisymmetric stretch normal mode motion at  $1494$   $\text{cm}^{-1}$ , we performed a scan along this ground-state normal mode, computing both the B3LYP LR-TDDFT and PIMOM energy gaps and oscillator strengths, shown in Figure 4. The inset of Figure 4a shows the normal mode vectors

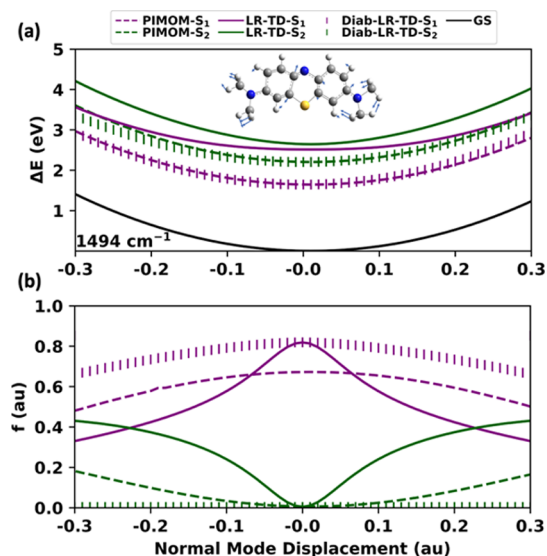


**Figure 4.** B3LYP potential surface scans of the ground state,  $S_1$ , and  $S_2$  states along the ground-state  $B_2$  antisymmetric stretch normal mode coordinate. (a) Adiabatic LR-TDDFT PESs are shown in solid lines, diabatic LR-TDDFT PESs are shown in vertical dashed lines and are shifted down in energy, PIMOM PESs are shown in horizontal dashed lines, and ground-state PES is drawn in black. The inset shows the displacement vectors for the ground-state  $1494$   $\text{cm}^{-1}$   $B_2$  asymmetric stretching mode. (b) LR-TDDFT and PIMOM oscillator strengths along the normal mode displacement.

corresponding to the atomic displacements with an animation of the normal mode shown in the Supporting Information. The PES scan in Figure 4a presents well-separated, nearly harmonic surfaces of the  $S_1$  and  $S_2$  states as computed with the PIMOM along the full normal mode displacement coordinate, unlike LR-TDDFT, where the surfaces are in close proximity at the minimum. Additionally, the shape of both the  $S_1$  and  $S_2$  LR-TDDFT PESs along this mode clearly deviates from harmonic behavior. The application of the quasi-diabatization procedure to the two LR states along this coordinate produces one lower



energy bright state and one higher energy dark state. To better compare the diabatic LR surfaces to the PIMOM surfaces, the diabatic LR  $S_1$  surface was shifted down in energy by 0.868 eV and the diabatic LR  $S_2$  surface was shifted down in energy by 0.440 eV to align with the PIMOM potentials at the ground-state minimum. The resulting  $S_1$  surfaces show nearly identical curvature along this normal mode, whereas the  $S_2$  diabatic LR surface is a bit wider than the  $S_2$  PIMOM surface, but still appears quite harmonic.

LR-TDDFT at the  $S_0$  minimum produces a bright  $S_1$  state with an oscillator strength of  $f \approx 0.8$ , whereas the  $S_2$  state is dark, see Figure 4b. As the atoms are displaced along this normal mode, the LR-TDDFT  $S_1$  state loses oscillator strength and the LR-TDDFT  $S_2$  state gains oscillator strength, showing that these two states mix together along this coordinate. At displacements of  $\pm 0.2$  au, the two states have nearly identical oscillator strengths of  $f \approx 0.4$ . The PIMOM oscillator strengths are not constant along this normal mode, but are much more consistent than the LR oscillator strengths, always producing a bright state for  $S_1$  and a darker state for  $S_2$ . Although the  $S_1$  oscillator strength does show a slight decrease and the  $S_2$  state a slight increase, the shape of the curves is not consistent with LR-TDDFT, suggesting a qualitatively distinct mixing of states for LR-TDDFT and for the PIMOM along this coordinate. The diabaticization of the LR  $S_1$  and  $S_2$  states yields oscillator strengths for  $S_1$  that very closely follow the trend of the PIMOM oscillator strengths. The  $S_2$  oscillator strengths do not follow the same trend, suggesting that the two-state quasi-diabatization procedure is missing some higher lying contributions for the  $S_2$  state.

Overall, this normal mode analysis supports our finding that the character of the  $S_1$  state is treated differently by LR-TDDFT compared to the PIMOM. The adiabatic LR-TD-B3LYP method leads to  $S_1$  and  $S_2$  state mixings in some regions of the methylene blue PES, both along this normal mode and at the  $S_1$  minimum, whereas the PIMOM maintains a more consistent  $S_1$  character. The good agreement between the diabaticized  $S_1$  LR surface and the PIMOM  $S_1$  surface, and the corresponding oscillator strengths, supports that the PIMOM may be a promising method for the generation of diabatic surfaces. Alternatively, the PIMOM B3LYP energy gap between  $S_1$  and  $S_2$  may be larger than with LR-TD-B3LYP, leading to less state mixing.

## 5. CONCLUSIONS

Calculating accurate optical spectra and excited-state surfaces from first principles is essential for connecting spectroscopic experiments to the electronic characterization and dynamics of chromophores. For this work, we chose the methylene blue chromophore because of its closely spaced  $S_1$  and  $S_2$  surfaces to compare the behavior of the widely used adiabatic LR-TDDFT approach with PIMOM  $\Delta$ SCF results for computing the excited states of methylene blue, then applied a number of approaches for simulating the vibronic spectra. Although the closely spaced excited states require a nonadiabatic treatment of three states for accurate spectral modeling, here they are used to showcase differences in a widely used and newly developed excited-state model, and two-state spectroscopic approaches.

We find that the adiabatic LR-TD-B3LYP approach yields  $S_1$  and  $S_2$  states that mix together near the  $S_1$  minimum. Although the  $S_1$  state is bright and the  $S_2$  state is dark at the ground-state minimum, the analysis of a key normal mode that strongly couples to the  $S_0 \rightarrow S_1$  transition shows that the  $S_2$  state borrows

intensity from  $S_1$  along this normal mode displacement, with  $S_1$  and  $S_2$  having nearly identical oscillator strengths at the  $S_1$  minimum. In contrast, the PIMOM produces states of consistent character across the PES, with a larger energy gap between  $S_1$  and  $S_2$ . The PIMOM also yields consistent character for both B3LYP and CAM-B3LYP  $S_1$  PESs and electron densities.

When applying these two excited-state methods to the computation of vibronic spectra using a Hessian computed at the  $S_1$  minimum, they yield very different results for methylene blue. The standard adiabatic Hessian LR-TD-B3LYP approach produces a very large vibronic shoulder in the spectrum due to a change in character of the PES at the  $S_1$  minimum because of the adiabatic treatment of the excited states. The spectra generated from LR-TD-B3LYP with a vertical gradient or an AIMD trajectory-based approach differ significantly from the adiabatic Hessian LR-TD3LYP approach, with no large vibronic shoulder. Large changes in the spectra with the second- and third-order truncation of the cumulant expansion using the LR-TD-B3LYP  $S_1$ -parametrized GBOM suggest substantial changes in PES curvature or a large Duschinsky rotation matrix, with large mixing of normal mode coordinates, possibly caused by the decrease in symmetry going from the  $S_0$   $C_{2v}$  to the LR-TD-B3LYP  $S_1$   $C_s$  minimum. In contrast, if the PIMOM is used to compute the  $S_1$  minimum and corresponding Hessian and normal modes, the resulting vibronic spectrum is in excellent agreement with the vertical gradient and AIMD trajectory-based approaches, showing that all of these methods have a consistent treatment of the  $S_1$  state in the region of the vertical excitation and at the PIMOM  $S_1$  minimum. Switching from the B3LYP to the CAM-B3LYP functional increases the gap between the  $S_1$  and  $S_2$  states, with the adiabatic Hessian LR-TDDFT, PIMOM, and AIMD trajectory-based approaches all producing spectra in good agreement.

The large differences between the TD-B3LYP adiabatic Hessian and vertical gradient methods suggest the breakdown of the Born–Oppenheimer or harmonic approximation in the region of the LR-TD-B3LYP  $S_1$  minimum. Indeed, the need for including nonadiabatic effects is supported by a recent study by some of the authors of solvated methylene blue that showed that there is significant population transfer from the  $S_1$  state to the  $S_2$  state upon photoexcitation, which is strongly coupled to the intensity of the vibronic shoulder.<sup>65</sup> Inclusion of this population transfer increases the vibronic shoulder, bringing the predicted spectrum more in line with the experimental spectrum of aqueously solvated methylene blue.

Here, we present additional diagnostics that signify the breakdown of the Born–Oppenheimer approximation and also present the PIMOM technique as a possible way to produce surfaces that appear diabatic in character. If the adiabatic Hessian method applied to both LR-TDDFT and PIMOM normal modes produces significantly different spectra, it is likely that the adiabatic LR-TDDFT minimum is in a region of state mixing, yielding surfaces with anharmonic curvature. The PIMOM produces excited states of consistent character and presents a promising alternative to LR-TDDFT for geometry optimization, frequency calculation, and the generation of diabatic surfaces. Further investigation is required to determine the PIMOM's suitability for computing diabatic surfaces in regions of crossings and for the computation of nonadiabatic couplings.

Our results here point to the challenge of using an adiabatic excited-state approach for the computation of some excited-

state properties, including the Hessian computed at an adiabatic excited-state minimum. Because adiabatic surfaces can change in character, the character of the state at the minimum may not accurately describe the system in the region of the vertical excitation. The state mixing seen here could be present with other adiabatic excited-state approaches and is not necessarily due to the inaccuracies of TDDFT. Although we here choose the methylene blue chromophore because it displays state mixing and thus will show large differences between adiabatic and diabatic Hessian approaches, such conical intersections are ubiquitous for organic chromophores and are likely to affect absorption spectra in other systems.

## ■ ASSOCIATED CONTENT

### SI Supporting Information

The Supporting Information is available free of charge at <https://pubs.acs.org/doi/10.1021/acs.jctc.1c01127>.

CAM-B3LYP density differences, analysis of second- and third-order cumulant spectra, asymmetric stretch normal mode animation, tables of adiabatic and vertical excitation energies, and optimized geometries (PDF)

## ■ AUTHOR INFORMATION

### Corresponding Authors

**Hrant P. Hratchian** – Department of Chemistry and Biochemistry, University of California Merced, Merced, California 95343, United States; [orcid.org/0000-0003-1436-5257](https://orcid.org/0000-0003-1436-5257); Email: [hhratchian@ucmerced.edu](mailto:hhratchian@ucmerced.edu)

**Christine M. Isborn** – Department of Chemistry and Biochemistry, University of California Merced, Merced, California 95343, United States; [orcid.org/0000-0002-3559-6129](https://orcid.org/0000-0002-3559-6129); Email: [cisborn@ucmerced.edu](mailto:cisborn@ucmerced.edu)

### Authors

**Ali Abou Taka** – Department of Chemistry and Biochemistry, University of California Merced, Merced, California 95343, United States; [orcid.org/0000-0003-0001-2813](https://orcid.org/0000-0003-0001-2813)

**Shao-Yu Lu** – Department of Chemistry and Biochemistry, University of California Merced, Merced, California 95343, United States

**Duncan Gowland** – Department of Physics, King's College London, London WC2R 2LS, United Kingdom

**Tim J. Zuehlsdorff** – Department of Chemistry, Oregon State University, Corvallis, Oregon 97331, United States

**Hector H. Corzo** – Department of Chemistry and Biochemistry, University of California Merced, Merced, California 95343, United States

**Aurora Pribram-Jones** – Department of Chemistry and Biochemistry, University of California Merced, Merced, California 95343, United States

**Liang Shi** – Department of Chemistry and Biochemistry, University of California Merced, Merced, California 95343, United States; [orcid.org/0000-0001-5033-3960](https://orcid.org/0000-0001-5033-3960)

Complete contact information is available at: <https://pubs.acs.org/doi/10.1021/acs.jctc.1c01127>

### Notes

The authors declare no competing financial interest.

## ■ ACKNOWLEDGMENTS

The data that support the findings of this study are available from the corresponding authors upon request. This work was

supported by the Department of Energy Basic Energy Sciences CTC and CPIMS Programs (grant no. DE-SC0019053). Calculations were performed using the MERCED computational resource, supported by the National Science Foundation Major Research Instrumentation Program (ACI-1429783).

## ■ REFERENCES

- (1) Ashford, D. L.; Gish, M. K.; Vannucci, A. K.; Brennaman, M. K.; Templeton, J. L.; Papanikolas, J. M.; Meyer, T. J. Molecular Chromophore-Catalyst Assemblies for Solar Fuel Applications. *Chem. Rev.* **2015**, *115*, 13006–13049.
- (2) Sarkar, K.; Dhara, K.; Nandi, M.; Roy, P.; Bhaumik, A.; Banerjee, P. Selective Zinc(II)-Ion Fluorescence Sensing by a Functionalized Mesoporous Material Covalently Grafted with a Fluorescent Chromophore and Consequent Biological Applications. *Adv. Funct. Mater.* **2009**, *19*, 223–234.
- (3) Fujimoto, K. J. Electronic Couplings and Electrostatic Interactions Behind the Light Absorption of Retinal Proteins. *Front. Mol. Biosci.* **2021**, *8*, 752700.
- (4) Linsley, C. S.; Quach, V. Y.; Agrawal, G.; Hartnett, E.; Wu, B. M. Visible light and near-infrared-responsive chromophores for drug delivery-on-demand applications. *Drug Delivery Transl. Res.* **2015**, *5*, 611–624.
- (5) Kanis, D. R.; Ratner, M. A.; Marks, T. J. Design and construction of molecular assemblies with large second-order optical nonlinearities. Quantum chemical aspects. *Chem. Rev.* **1994**, *94*, 195–242.
- (6) Robinson, B. H.; Salamin, Y.; Baeuerle, B.; Josten, A.; Ayata, M.; Koch, U.; Leuthold, J.; Dalton, L. R.; Johnson, L. E.; Elder, D. L.; Kocherzhenko, A. A.; Isborn, C. M.; Haffner, C.; Heni, W.; Hoessbacher, C.; Fedoryshyn, Y. Optimization of Plasmonic-Organic Hybrid Electro-Optics. *J. Lightwave Technol.* **2018**, *36*, 5036–5047.
- (7) Casida, M. E. Time-Dependent Density Functional Response Theory for Molecules. In *Recent Advances in Density Functional Methods*; World Scientific, 1995, pp 155–192. DOI: 10.1142/9789812830586\_0005
- (8) Bauernschmitt, R.; Ahlrichs, R. Treatment of electronic excitations within the adiabatic approximation of time dependent density functional theory. *Chem. Phys. Lett.* **1996**, *256*, 454–464.
- (9) Furche, F.; Ahlrichs, R. Adiabatic time-dependent density functional methods for excited state properties. *J. Chem. Phys.* **2002**, *117*, 7433–7447.
- (10) Parker, S. M.; Furche, F. Response Theory and Molecular Properties. In *Frontiers of Quantum Chemistry*; Springer Singapore: Singapore, 2018, pp 69–86. DOI: 10.1007/978-981-10-5651-2\_4
- (11) Laurent, A. D.; Jacquemin, D. TD-DFT benchmarks: A review. *Int. J. Quantum Chem.* **2013**, *113*, 2019–2039.
- (12) Maitra, N. T.; Zhang, F.; Cave, R. J.; Burke, K. Double excitations within time-dependent density functional theory linear response. *J. Chem. Phys.* **2004**, *120*, 5932–5937.
- (13) Cave, R. J.; Zhang, F.; Maitra, N. T.; Burke, K. A dressed TDDFT treatment of the 21Ag states of butadiene and hexatriene. *Chem. Phys. Lett.* **2004**, *389*, 39–42.
- (14) Levine, B. G.; Ko, C.; Quenneville, J.; Martínez, T. J. Conical intersections and double excitations in time-dependent density functional theory. *Mol. Phys.* **2006**, *104*, 1039–1051.
- (15) Elliott, P.; Goldson, S.; Canahui, C.; Maitra, N. T. Perspectives on double-excitations in TDDFT. *Chem. Phys.* **2011**, *391*, 110–119.
- (16) Corzo, H. H.; Abou Taka, A.; Pribram-Jones, A.; Hratchian, H. P. Using projection operators with maximum overlap methods to simplify challenging self-consistent field optimization. *J. Comput. Chem.* **2022**, *43*, 382–390.
- (17) Abou Taka, A.; Corzo, H.; Pribram-Jones, A.; Hratchian, H. Good Vibrations: Calculating Excited State Frequencies Using Ground State Self-Consistent Field Models. *ChemRxiv* **2021**, 1–28, DOI: 10.26434/chemrxiv-2021-cch5r.
- (18) Gilbert, A. T. B.; Besley, N. A.; Gill, P. M. W. Self-consistent field calculations of excited states using the maximum overlap method (MOM). *J. Phys. Chem. A* **2008**, *112*, 13164–13171.

- (19) Zhan, C.-G. Maximum overlap method and the bond strength. *Int. J. Quantum Chem.* **1987**, *32*, 1–11.
- (20) Maksić, Z. B.; Eckert-Maksić, M.; Randić, M. Correlation between CH and CC spin-spin coupling constants and s character of hybrids calculated by the maximum overlap method. *Theor. Chim. Acta* **1971**, *22*, 70–79.
- (21) Cioslowski, J.; Challacombe, M. Maximum similarity orbitals for analysis of the electronic excited states. *Int. J. Quantum Chem.* **1991**, *40*, 81–93.
- (22) Hait, D.; Head-Gordon, M. Excited state orbital optimization via minimizing the square of the gradient: General approach and application to singly and doubly excited states via density functional theory. *J. Chem. Theory Comput.* **2020**, *16*, 1699–1710.
- (23) Carter-Fenk, K.; Herbert, J. M. State-Targeted Energy Projection: A Simple and Robust Approach to Orbital Relaxation of Non-Aufbau Self-Consistent Field Solutions. *J. Chem. Theory Comput.* **2020**, *16*, 5067–5082.
- (24) Levi, G.; Ivanov, A. V.; Jónsson, H. Variational Density Functional Calculations of Excited States via Direct Optimization. *J. Chem. Theory Comput.* **2020**, *16*, 6968–6982.
- (25) Pradhan, E.; Sato, K.; Akimov, A. V. Non-adiabatic molecular dynamics with  $\Delta$ SCF excited states. *J. Phys.: Condens. Matter* **2018**, *30*, 484002.
- (26) Karpinski, N.; Ramos, P.; Pavanello, M. Capturing multi-reference excited states by constrained-density-functional theory. *Phys. Rev. A* **2020**, *101*, 032510.
- (27) Malis, M.; Lubert, S. Trajectory Surface Hopping Nonadiabatic Molecular Dynamics with Kohn–Sham  $\Delta$ SCF for Condensed-Phase Systems. *J. Chem. Theory Comput.* **2020**, *16*, 4071–4086.
- (28) Ramos, P.; Pavanello, M. Nonadiabatic couplings from a variational excited state method based on constrained DFT. *J. Chem. Phys.* **2021**, *154*, 014110.
- (29) Schmerwitz, Y. L. A.; Ivanov, A. V.; Jónsson, E. Ö.; Jónsson, H.; Levi, G. Variational Density Functional Calculations of Excited States: Conical Intersection and Avoided Crossing in Ethylene Bond Twisting. **2022**, arXiv:2203.07197. arXiv preprint.
- (30) Besley, N. A.; Gilbert, A. T. B.; Gill, P. M. W. Self-consistent-field calculations of core excited states. *J. Chem. Phys.* **2009**, *130*, 124308.
- (31) Deng, J.; Gilbert, A. T. B.; Gill, P. M. W. Rydberg states of the helium atom. *Int. J. Quantum Chem.* **2009**, *109*, 1915–1919.
- (32) Mason, J. L.; Harb, H.; Abou Taka, A.; Huizenga, C. D.; Corzo, H. H.; Hratchian, H. P.; Jarrold, C. C. New Photoelectron-Valence Electron Interactions Evident in the Photoelectron Spectrum of Gd<sub>2</sub>O<sub>3</sub>. *J. Phys. Chem. A* **2021**, *125*, 9892–9903.
- (33) Mason, J. L.; Harb, H.; Taka, A. A.; McMahan, A. J.; Huizenga, C. D.; Corzo, H.; Hratchian, H. P.; Jarrold, C. C. Photoelectron Spectra of Gd<sub>2</sub>O<sub>3</sub>- and Nonmonotonic Photon-Energy-Dependent Variations in Populations of Close-Lying Neutral States. *J. Phys. Chem. A* **2021**, *125*, 857–866.
- (34) Tolbatov, I.; Chipman, D. M. Comparative study of Gaussian basis sets for calculation of core electron binding energies in first-row hydrides and glycine. *Theor. Chem. Acc.* **2014**, *133*, 1560.
- (35) Tolbatov, I.; Chipman, D. M. Benchmarking density functionals and Gaussian basis sets for calculation of core-electron binding energies in amino acids. *Theor. Chem. Acc.* **2017**, *136*, 82.
- (36) Cabral do Couto, P.; Hollas, D.; Slaviček, P. On the performance of optimally tuned range-separated hybrid functionals for x-ray absorption modeling. *J. Chem. Theory Comput.* **2015**, *11*, 3234–3244.
- (37) Coons, M. P.; Herbert, J. M. Quantum chemistry in arbitrary dielectric environments: Theory and implementation of nonequilibrium Poisson boundary conditions and application to compute vertical ionization energies at the air/water interface. *J. Chem. Phys.* **2018**, *148*, 222834.
- (38) Hanson-Heine, M. W. D.; George, M. W.; Besley, N. A. Basis sets for the calculation of core-electron binding energies. *Chem. Phys. Lett.* **2018**, *699*, 279–285.
- (39) Hanson-Heine, M. W. D.; George, M. W.; Besley, N. A. A scaled CIS(D) based method for the calculation of valence and core electron ionization energies. *J. Chem. Phys.* **2019**, *151*, 034104.
- (40) Hanson-Heine, M. W. D.; George, M. W.; Besley, N. A. Calculating excited state properties using Kohn-Sham density functional theory. *J. Chem. Phys.* **2013**, *138*, 064101.
- (41) Hanson-Heine, M. W. D.; Wriglesworth, A.; Uroos, M.; Calladine, J. A.; Murphy, T. S.; Hamilton, M.; Clark, I. P.; Towrie, M.; Dowden, J.; Besley, N. A.; et al. Calculating singlet excited states: Comparison with fast time-resolved infrared spectroscopy of coumarins. *J. Chem. Phys.* **2015**, *142*, 154119.
- (42) Hanson-Heine, M. W. D.; Calladine, J. A.; Yang, J.; Towrie, M.; Horvath, R.; Besley, N. A.; George, M. W. A combined time-resolved infrared and density functional theory study of the lowest excited states of 9-fluorenone and 2-naphthaldehyde. *Chem. Phys.* **2018**, *512*, 44–52.
- (43) Berger, R.; Fischer, C.; Klessinger, M. Calculation of the vibronic fine structure in electronic spectra at higher temperatures. I. Benzene and pyrazine. *J. Phys. Chem. A* **1998**, *102*, 7157–7167.
- (44) Petrenko, T.; Neese, F. Analysis and prediction of absorption band shapes, fluorescence band shapes, resonance Raman intensities, and excitation profiles using the time-dependent theory of electronic spectroscopy. *J. Chem. Phys.* **2007**, *127*, 164319.
- (45) Baiardi, A.; Bloino, J.; Barone, V. General Time Dependent Approach to Vibronic Spectroscopy Including Franck-Condon, Herzberg-Teller, and Duschinsky Effects. *J. Chem. Theory Comput.* **2013**, *9*, 4097–4115.
- (46) Baiardi, A.; Bloino, J.; Barone, V. General formulation of vibronic spectroscopy in internal coordinates. *J. Chem. Phys.* **2016**, *144*, 084114.
- (47) Biczysko, M.; Bloino, J.; Santoro, F.; Barone, V. Time-Independent Approaches to Simulate Electronic Spectra Lineshapes: From Small Molecules to Macrosystems. In *Computational Strategies for Spectroscopy*; John Wiley & Sons, Ltd, 2011; pp 361–443. Chapter 8.
- (48) Duschinsky, F. *Acta Physicochim. URSS.* **1937**, *7*, 551.
- (49) Macak, P.; Luo, Y.; Ågren, H. Simulations of vibronic profiles in two-photon absorption. *Chem. Phys. Lett.* **2000**, *330*, 447–456.
- (50) Mukazhanova, A.; Trerayapiwat, K. J.; Mazaheripour, A.; Wardrip, A. G.; Frey, N. C.; Nguyen, H.; Gorodetsky, A. A.; Sharifzadeh, S. Accurate first-principles calculation of the vibronic spectrum of stacked perylene tetracarboxylic acid diimides. *J. Phys. Chem. A* **2020**, *124*, 3055–3063.
- (51) Hazra, A.; Chang, H. H.; Nooijen, M. First principles simulation of the UV absorption spectrum of ethylene using the vertical Franck-Condon approach. *J. Chem. Phys.* **2004**, *121*, 2125–2136.
- (52) Hazra, A.; Nooijen, M. Vibronic coupling in the excited cationic states of ethylene: Simulation of the photoelectron spectrum between 12 and 18eV. *J. Chem. Phys.* **2005**, *122*, 204327.
- (53) Avila Ferrer, F. J.; Santoro, F. Comparison of vertical and adiabatic harmonic approaches for the calculation of the vibrational structure of electronic spectra. *Phys. Chem. Chem. Phys.* **2012**, *14*, 13549–13563.
- (54) Mukamel, S. *Principles of Nonlinear Optical Spectroscopy*; Oxford University Press: New York, 1995.
- (55) Zuehlsdorff, T. J.; Montoya-Castillo, A.; Napoli, J. A.; Markland, T. E.; Isborn, C. M. Optical spectra in the condensed phase: Capturing anharmonic and vibronic features using dynamic and static approaches. *J. Chem. Phys.* **2019**, *151*, 074111.
- (56) Zuehlsdorff, T. J.; Shedje, S. V.; Lu, S.-Y.; Hong, H.; Aguirre, V. P.; Shi, L.; Isborn, C. M. Vibronic and Environmental Effects in Simulations of Optical Spectroscopy. *Annu. Rev. Phys. Chem.* **2021**, *72*, 165–188 PMID: 33395546.
- (57) Bader, J. S.; Berne, B. J. Quantum and classical relaxation rates from classical simulations. *J. Chem. Phys.* **1994**, *100*, 8359.
- (58) Egorov, S. A.; Everitt, K. F.; Skinner, J. L. Quantum Dynamics and Vibrational Relaxation. *J. Phys. Chem. A* **1999**, *103*, 9494–9499.
- (59) Kim, H.; Rossky, P. J. Evaluation of Quantum Correlation Functions from Classical Data. *J. Phys. Chem. B* **2002**, *106*, 8240.
- (60) Valteau, S.; Eisfeld, A.; Aspuru-Guzik, A. On the alternatives for bath correlators and spectral densities from mixed quantum-classical simulations. *J. Chem. Phys.* **2012**, *137*, 224103.
- (61) Zuehlsdorff, T.; Hong, H.; Shi, L.; Isborn, C. Nonlinear Spectroscopy in the Condensed Phase: The Role of Duschinsky



- Rotations and Third Order Cumulant Contributions. *J. Chem. Phys.* **2020**, *153*, 044127.
- (62) Zuehlsdorff, T. J.; Hong, H.; Shi, L.; Isborn, C. M. Influence of Electronic Polarization on the Spectral Density. *J. Phys. Chem. B* **2020**, *124*, 531–543.
- (63) Lu, S.-Y.; Zuehlsdorff, T. J.; Hong, H.; Aguirre, V. P.; Isborn, C. M.; Shi, L. The Influence of Electronic Polarization on Nonlinear Optical Spectroscopy. *J. Phys. Chem. B* **2021**, *125*, 12214–12227.
- (64) de Queiroz, T. B.; de Figueroa, E. R.; Coutinho-Neto, M. D.; Maciel, C. D.; Tapavicz, E.; Hashemi, Z.; Leppert, L. First principles theoretical spectroscopy of methylene blue: Between limitations of time-dependent density functional theory approximations and its realistic description in the solvent. *J. Chem. Phys.* **2021**, *154*, 044106.
- (65) Dunnett, A. J.; Gowland, D.; Isborn, C. M.; Chin, A. W.; Zuehlsdorff, T. J. Influence of non-adiabatic effects on linear absorption spectra in the condensed phase: Methylene blue. *J. Chem. Phys.* **2021**, *155*, 144112.
- (66) Barca, G. M. J.; Gilbert, A. T. B.; Gill, P. M. W. Simple Models for Difficult Electronic Excitations. *J. Chem. Theory Comput.* **2018**, *14*, 1501–1509.
- (67) Barca, G. M.; Gilbert, A. T.; Gill, P. M. *Communication: Hartree-Fock Description of Excited States of H<sub>2</sub>*; American Institute of Physics, 2014.
- (68) Hratchian, H. P. Communication: An efficient analytic gradient theory for approximate spin projection methods. *J. Chem. Phys.* **2013**, *138*, 101101.
- (69) Thompson, L. M.; Hratchian, H. P. Second derivatives for approximate spin projection methods. *J. Chem. Phys.* **2015**, *142*, 054106.
- (70) Thompson, L. M.; Hratchian, H. P. Modeling the Photoelectron Spectra of MoNbO<sub>2</sub>—Accounting for Spin Contamination in Density Functional Theory. *J. Phys. Chem. A* **2015**, *119*, 8744–8751.
- (71) Sheng, X.; Thompson, L. M.; Hratchian, H. P. Assessing the Calculation of Exchange Coupling Constants and Spin Crossover Gaps Using the Approximate Projection Model to Improve Density Functional Calculations. *J. Chem. Theory Comput.* **2019**, *16*, 154–163.
- (72) Bao, P.; Hettich, C. P.; Shi, Q.; Gao, J. Block-Localized Excitation for Excimer Complex and Diabatic Coupling. *J. Chem. Theory Comput.* **2021**, *17*, 240–254 PMID: 33370101.
- (73) Simons, J. One-Electron Electron–Molecule Potentials Consistent with ab Initio Møller–Plesset Theory†. *J. Phys. Chem. A* **2010**, *114*, 8631–8643.
- (74) Cerezo, J.; Avila Ferrer, F. J.; Prampolini, G.; Santoro, F. Modeling Solvent Broadening on the Vibronic Spectra of a Series of Coumarin Dyes. From Implicit to Explicit Solvent Models. *J. Chem. Theory Comput.* **2015**, *11*, 5810–5825.
- (75) Doktorov, E. V.; Malkin, I. A.; Man'ko, V. I. Dynamical symmetry of vibronic transitions in polyatomic molecules and the Franck-Condon principle. *J. Mol. Spectrosc.* **1975**, *56*, 1–20.
- (76) Santoro, F.; Lami, A.; Improtà, R.; Bloino, J.; Barone, V. Effective method for the computation of optical spectra of large molecules at finite temperature including the Duschinsky and Herzberg-Teller effect: The Q<sub>x</sub> band of porphyrin as a case study. *J. Chem. Phys.* **2008**, *128*, 224311.
- (77) de Souza, B.; Neese, F.; Izsák, R. On the theoretical prediction of fluorescence rates from first principles using the path integral approach. *J. Chem. Phys.* **2018**, *148*, 034104.
- (78) Anda, A.; De Vico, L.; Hansen, T.; Abramavičius, D. Absorption and Fluorescence Lineshape Theory for Polynomial Potentials. *J. Chem. Theory Comput.* **2016**, *12*, 5979–5989.
- (79) Meyer, H.-D.; Manthe, U.; Cederbaum, L. S. The multi-configurational time-dependent Hartree approach. *Chem. Phys. Lett.* **1990**, *165*, 73–78.
- (80) Schröder, F. A. Y. N.; Turban, D. H. P.; Musser, A. J.; Hine, N. D. M.; Chin, A. W. Tensor network simulation of multi-environmental open quantum dynamics via machine learning and entanglement renormalisation. *Nat. Commun.* **2019**, *10*, 1062.
- (81) Frisch, M. J.; Pople, J. A.; Binkley, J. S. Self-consistent molecular orbital methods 25. Supplementary functions for Gaussian basis sets. *J. Chem. Phys.* **1984**, *80*, 3265–3269.
- (82) Seeger, R.; Pople, J. A. Self-consistent molecular orbital methods. XVIII. Constraints and stability in Hartree-Fock theory. *J. Chem. Phys.* **1977**, *66*, 3045–3050.
- (83) Bauernschmitt, R.; Ahlrichs, R. Stability analysis for solutions of the closed shell Kohn-Sham equation. *J. Chem. Phys.* **1996**, *104*, 9047–9052.
- (84) Casida, M. E.; Jamorski, C.; Casida, K. C.; Salahub, D. R. Molecular excitation energies to high-lying bound states from time-dependent density-functional response theory: Characterization and correction of the time-dependent local density approximation ionization threshold. *J. Chem. Phys.* **1998**, *108*, 4439–4449.
- (85) Stratmann, R. E.; Scuseria, G. E.; Frisch, M. J. An efficient implementation of time-dependent density-functional theory for the calculation of excitation energies of large molecules. *J. Chem. Phys.* **1998**, *109*, 8218–8224.
- (86) Frisch, M. J.; Trucks, G. W.; Schlegel, H. B.; Scuseria, G. E.; Robb, M. A.; Cheeseman, J. R.; Scalmani, G.; Barone, V.; Petersson, G. A.; Nakatsuji, H.; Li, X.; Caricato, M.; Marenich, A. V.; Bloino, J.; Janesko, B. G.; Gomperts, R.; Mennucci, B.; Hratchian, H. P.; Ortiz, J. V.; Izmaylov, A. F.; Sonnenberg, J. L.; Williams-Young, D.; Ding, F.; Lipparini, F.; Egidi, F.; Goings, J.; Peng, B.; Petrone, A.; Henderson, T.; Ranasinghe, D.; Zakrzewski, V. G.; Gao, J.; Rega, N.; Zheng, G.; Liang, W.; Hada, M.; Ehara, M.; Toyota, K.; Fukuda, R.; Hasegawa, J.; Ishida, M.; Nakajima, T.; Honda, Y.; Kitao, O.; Nakai, H.; Vreven, T.; Throssell, K.; Montgomery, J. A., Jr.; Peralta, J. E.; Ogliaro, F.; Bearpark, M. J.; Heyd, J. J.; Brothers, E. N.; Kudin, K. N.; Staroverov, V. N.; Keith, T. A.; Kobayashi, R.; Normand, J.; Raghavachari, K.; Rendell, A. P.; Burant, J. C.; Iyengar, S. S.; Tomasi, J.; Cossi, M.; Millam, J. M.; Klene, M.; Adamo, C.; Cammi, R.; Ochterski, J. W.; Martin, R. L.; Morokuma, K.; Farkas, O.; Foresman, J. B.; Fox, D. J. *Gaussian Development Version, Revision J.05*; Gaussian Inc.: Wallingford CT, 2020.
- (87) Thompson, L. M.; Harb, H.; Hratchian, H. P. Natural ionization orbitals for interpreting electron detachment processes. *J. Chem. Phys.* **2016**, *144*, 204117.
- (88) Harb, H.; Hratchian, H. P. ΔSCF Dyson orbitals and pole strengths from natural ionization orbitals. *J. Chem. Phys.* **2021**, *154*, 084104.
- (89) Harb, H.; Hratchian, H. P. Natural ionization orbitals. 2020; <https://github.com/HratchianGroup/niorep>, (Last accessed on June 15, 2021).
- (90) Martin, R. L. Natural transition orbitals. *J. Chem. Phys.* **2003**, *118*, 4775–4777.
- (91) Sonnenberg, J. L.; Schlegel, H. B.; Hratchian, H. P. Spin Contamination in Inorganic Chemistry Calculations. In *Encyclopedia of Inorganic and Bioinorganic Chemistry*; American Cancer Society, 2011; pp 173–186.
- (92) Saito, T.; Nishihara, S.; Kataoka, Y.; Nakanishi, Y.; Matsui, T.; Kitagawa, Y.; Kawakami, T.; Okumura, M.; Yamaguchi, K. Transition state optimization based on approximate spin-projection (AP) method. *Chem. Phys. Lett.* **2009**, *483*, 168–171.
- (93) Saito, T.; Ito, A.; Watanabe, T.; Kawakami, T.; Okumura, M.; Yamaguchi, K. Performance of the coupled cluster and DFT methods for through-space magnetic interactions of nitroxide dimer. *Chem. Phys. Lett.* **2012**, *542*, 19–25.
- (94) Ferré, N.; Guihéry, N.; Malrieu, J.-P. Spin decontamination of broken-symmetry density functional theory calculations: deeper insight and new formulations. *Phys. Chem. Chem. Phys.* **2015**, *17*, 14375–14382.
- (95) Thompson, L. M.; Hratchian, H. P. Spin projection with double hybrid density functional theory. *J. Chem. Phys.* **2014**, *141*, 034108.
- (96) Hratchian, H. P.; Schlegel, H. B. Finding minima, transition states, and following reaction pathways on ab initio potential energy surfaces. *Theory and Applications of Computational Chemistry: The First 40 Years*; Dykstra, CE, 2005, pp 195–249. DOI: 10.1016/b978-044451719-7/50053-6

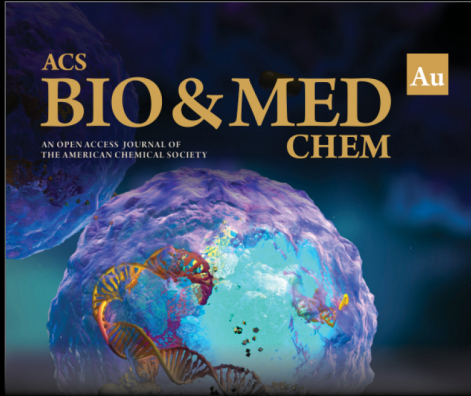
(97) Schaefer, H. F., III; Yamaguchi, Y. A new dimension to quantum chemistry: Theoretical methods for the analytic evaluation of first, second, and third derivatives of the molecular electronic energy with respect to nuclear coordinates. *J. Mol. Struct.: THEOCHEM* **1986**, *135*, 369–390.

(98) Stratmann, R. E.; Burant, J. C.; Scuseria, G. E.; Frisch, M. J. Improving harmonic vibrational frequencies calculations in density functional theory. *J. Chem. Phys.* **1997**, *106*, 10175–10183.

(99) Santoro, F.; Improta, R.; Lami, A.; Bloino, J.; Barone, V. Effective method to compute Franck-Condon integrals for optical spectra of large molecules in solution. *J. Chem. Phys.* **2007**, *126*, 084509.

(100) Zuehlsdorff, T. J. MolSpeckPy: Spectroscopy python code, available on Github: [https://github.com/tjz21/Spectroscopy\\_python\\_code](https://github.com/tjz21/Spectroscopy_python_code), (Last accessed on June 15, 2021).


(101) Medders, G. R.; Alguire, E. C.; Jain, A.; Subotnik, J. E. Ultrafast Electronic Relaxation through a Conical Intersection: Nonadiabatic Dynamics Disentangled through an Oscillator Strength-Based Diabatization Framework. *J. Phys. Chem. A* **2017**, *121*, 1425–1434.




ACS  
**BIO & MED** Au  
CHEM  
AN OPEN ACCESS JOURNAL OF  
THE AMERICAN CHEMICAL SOCIETY

Editor-in-Chief: **Prof. Shelley D. Minteer**, University of Utah, USA

Deputy Editor  
**Prof. Squire J. Booker**  
Pennsylvania State University, USA

**Open for Submissions** 

pubs.acs.org/biomedchemau  ACS Publications  
Most Trusted. Most Cited. Most Read.